2011 IEEE/RSJ International Conference on
Intelligent Robots and Systems
September 25-30, 2011. San Francisco, CA, USA

A Friction Differential and Cable Transmission Design for a 3-DOF Haptic Device with Spherical Kinematics

Reuben Brewer, Adam Leeper, and J. Kenneth Salisbury

Abstract— **We present a new mechanical design for a 3-DOF haptic device with spherical kinematics (pitch, yaw, and prismatic radial). All motors are grounded in the base to decrease inertia and increase compactness near the user's hand. An aluminum-aluminum friction differential allows for actuation of pitch and yaw with mechanical robustness while allowing a cable transmission to route through its center. This novel cabling system provides simple, compact, and high-performance actuation of the radial DOF independent of motions in pitch and yaw. We show that the device's capabilities are suitable for general haptic rendering, as well as specialized applications of spherical kinematics such as laparoscopic surgery simulation.**

I. INTRODUCTION

As the application of haptics becomes more common and widespread, a need arises for haptic device designs which exhibit a slim form factor, are suitable over a range of scales, are mechanically robust, and are capable of general haptic rendering as opposed to specialized applications. Spherical kinematics can be used to achieve such slim, scalable designs by concentrating the motors and transmission in the base of the device and leaving a slender, single-link connection to the user's hand. Ideally, the base of the spherical haptic device can be stowed outside of the user's view, and the single link that connects to the user's hand can be easily stowed, unlike a non-spherical device that connects to the user's hand via several links. While there are many different haptic devices with spherical kinematics, much remains to be desired in terms of the simplicity, compactness, and robustness of their mechanical design. Further, the usage of spherical kinematics has generally been limited to haptic devices aimed at specific applications, such as gaming and laparoscopic simulation, rather than general haptic rendering.

In this paper, we present a new mechanical design for a spherical haptic device with pitch, yaw, and radial degree-of-freedom (DOF). Our design has a compact base and slim form factor that can be scaled to large devices and small devices. We achieve low inertia and high compactness/scalability through use of grounded motors and the novel combination of a friction differential with a new way of routing a cable transmission through the differential to a prismatic DOF. The simplicity of our design makes the device easy to manufacture, assemble, and maintain, providing reliable operation. The workspace and force-rendering capabilities of our device make it suitable for general haptic-rendering, and the novel mechanical design improves on existing designs for specific applications of spherical kinematics, such as laparoscopic surgery simulation.

R. Brewer and A. Leeper are with the Department of Mechanical Engineering, Stanford University, Stanford, CA, USA rdbrewer, aleeper@stanford.edu

J.K. Salisbury is with the Departments of Computer Science and Surgery, Stanford University, Stanford, CA, USA jks@robotics.stanford.edu

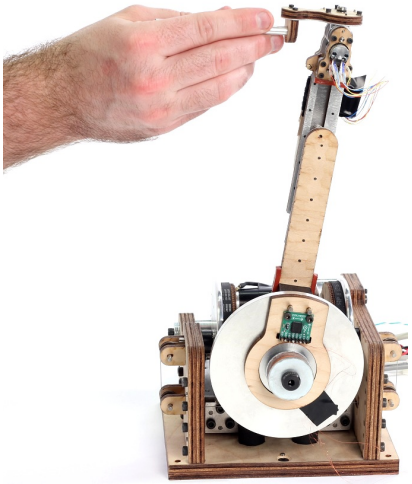

Fig. 1: Our 3-DOF spherical haptic device.

In the following sections, we begin with a discussion of related work. We then describe the mechanical design, including considerations for the friction differential, the prismatic radial DOF, and the wrist gimbal. We anaylze characteristics and capabilities of the device, including workspace, resolution, foward kinematics, jacobian, gravity compensation, maximum force, friction, dynamic range, and effective mass. We conclude with a discussion of future work.

II. RELATED WORK

The term "spherical kinematics" actually covers several distinct kinematic combinations of pitch, yaw, roll, and a prismatic, radial DOF. The simplest of such devices, such as [1] and the Impulse Engine 2000 (Immersion Corporation, San Jose, CA), are essentially 2-DOF, force-feedback joysticks that apply torques about pitch and yaw while keeping the user's hand on the surface of a fixed sphere. The SHaDe haptic device [2] has 3 DOF that apply torques in roll, pitch, and yaw centered about the user's hand. Neither of these kinematic configurations allows for translation and force-rendering in arbitrary 3D space, making these devices unsuitable for the type of general haptic rendering possible with devices like the Phantom [3] or Delta [4]. The addition of a prismatic, radial DOF is critical to this general usability.

Two spherical devices that incorporate a radial DOF have

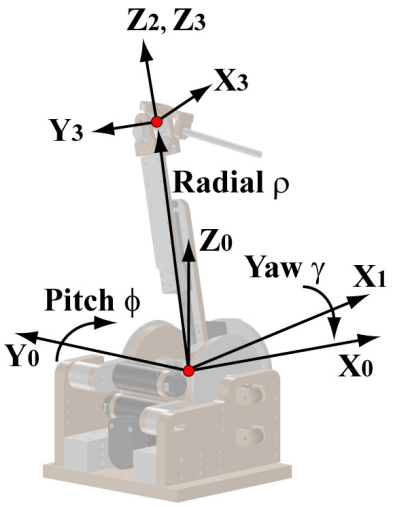

Fig. 2: The motion variables are pitch ϕ (rotation about $\mathbf{Y_0}$), yaw γ (rotation about $\mathbf{X_1}$), and radial ρ (translation along $\mathbf{Z_2}$).

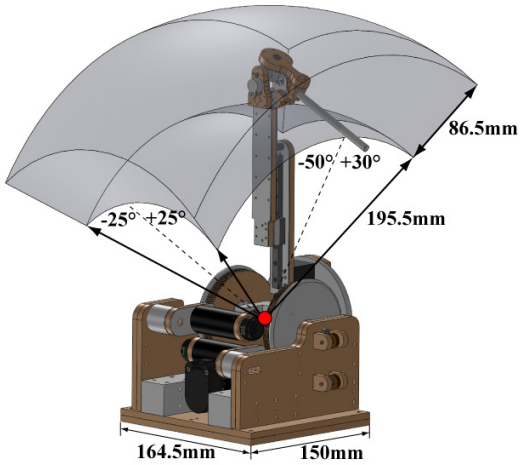

Fig. 3: The device workspace is a segment of a spherical shell. Pitch is on the range $\phi \in [-50°, +30°]$, yaw is on the range $\gamma \in [-25°, +25°]$, and extension is on the range $\rho \in [0, 86.5]$mm. The radius of the inner surface of the workspace is 195.5mm

been developed for general haptic interaction. In [5], the radial DOF was driven by a motor that that was attached to the moving pitch/yaw gimbal mechanism and converted rotary to linear motion via a cable. In [6], the radial DOF was driven by a cable that was routed in a flexible sleeve from a grounded motor. However, the friction between the sleeve and cable averaged 9N, uncompensated, and required active compensation based on force measurements to reduce the friction to a little under 1N.

A spherical haptic device with a radial DOF is ideally-suited to simulation of laparoscopic and natural orifice surgeries. In such procedures, the surgeon inserts a rigid tool through a small incision (or naturally-ocurring orifice) to gain access to internal structures. To prevent tearing of the entry point, the tool must be constrained to rotate about and translate through the entry point, which is essentially a spherical pivot with radial insertion. Although a haptic device with non-spherical kinematics could be used to simulate such a procedure, we can greatly reduce the physical size of the simulator and the forces that must be generated by using spherical kinematics. One such device is a 4-DOF simulator for vaginal hysterectomies [7]. It uses two grounded motors to actuate pitch and yaw and two motors mounted on the moving mechanism to actuate roll about the instrument's axis and the prismatic, radial DOF via friction rollers. Another such simulator is the LaparoscopyVR Surgical Simulator (CAE Healthcare, Montréal, Quebéc) [8], which simulates abdominal laparoscopic surgeries with the same 4 degrees of freedom as in [7]. It grounds all 4 motors for reduced inertia and uses a complicated system of cables that route through the entire mechanism to actuate each DOF.

We believe that our device improves on these previous designs in several respects. In the above devices, actuation of the radial DOF was accomplished either by a motor attached to moving links [5] [7], thereby hurting inertia and compactness, via a transmission with high frictional losses [6], or via a very complex cable transmission [8]. By grounding all motors, we have improved the inertial properties and compactness/form-factor. Our novel combination of an aluminum-aluminum friction differential and a new cable-routing technique produces a simpler, more robust transmission. We envision that our device could be a viable competitor to commercially-available devices for general haptic rendering, as well as spherical-specific applications.

III. MECHANICAL DESIGN

The basic structure of our device is shown in Figure 1. Kinematically, it can be described as a 3-DOF RRP manipulator, where the rotational motions move the tip of an arm along the surface of a sphere, and linear extension of the arm changes the radius of that sphere.

We use the following definitions of frames and motions: (refer to Figure 2):

- The base frame $\{0\}$ with origin O_0 is placed at the center of rotation of the differential. We align $\mathbf{X_0}$ to the user's right, $\mathbf{Y_0}$ forward, and $\mathbf{Z_0}$ up.
- Frame $\{1\}$ is colocated with frame $\{0\}$, and then rotated by an angle ϕ (pitch) about $\mathbf{Y_0}$.
- Frame $\{2\}$ is colocated with frame $\{1\}$, and then rotated by an angle γ (yaw) about $\mathbf{X_1}$.
- Frame $\{3\}$ is aligned with frame $\{2\}$ but offset along $\mathbf{Z_2}$ to coincide with the end-effector. The radial variable is ρ; the distance between the frame origins O_0 and O_3 is $r = \rho + R_e$, where $R_e = 195.5mm$.
- The home position of the device ($\phi = 0$, $\gamma = 0$, $\rho = 0$) is when the arm is vertical and fully retracted.

A. Friction Differential

We used a friction differential to achieve pitch and yaw, as shown in Figure 4, for a variety of benefits.

- The parallel structure allows for a smaller, stiffer mechanism than does a serial mechanism.
- Both motors are grounded easily, lowering the inertia of the mechanism and increasing compactness.
- The center of rotation of the differential is hollow, allowing for actuation cables to be routed through it.
- The use of a friction drive results in zero backlash, fewer machined parts, easier assembly, and a more robust mechanism because the wheels slip under excess torque rather than breaking cables or gear teeth as would happen in a cable or gear differential.

The driven plate is preloaded against the drive wheels by means of an adjustable rubber spring. This spring sets the normal force on the wheels, and, thence, the friction and torque transfer capacity of the wheels. Once we have determined the wheel material and desired preload, the only way to increase torque transfer capacity is to increase the diameter of the drive wheels, in the case of pitch, and increase the distance between the drive wheels, in the case of yaw. We arrived at our specific diameters by setting a preload for which the bearings still rotated smoothly and increasing the diameter until the slippage force was double what we wished to transfer to meet our peak force goal of 8N. We used a stationary Maxon RE-25 motor and a belt transmission with a 12:130 (1/10.833) reduction to drive each differential wheel. We used belts as the transmission for their ease of installation. A US Digital 360 CPR encoder on each motor yielded a resolution of 0.016° ($2.8 \cdot 10^{-4}$ rad) in both pitch and yaw.

The selection of drive wheel profile and material is critical for optimizing the differential's performance. We considered three different profiles for the drive wheels, as shown in Figure 4. The simplest profile is a flat cylindrical surface. However, because the wheels and drive plate contact along a line, there is sliding motion at the interface which produces high friction loss. A better approach is a point contact between the wheels, which results in pure rolling and no sliding. The simplest wheel profile that achieves a point contact is a sharp wedge. However, such a sharp, thin profile tends to deform easily and cut into the driven plate, resulting in a potentially uneven groove that increases friction loss. The best-performing profile is semicircular, or "round", because it provides a point contact that does not deform or dull easily and does not harm the driven plate.

The material parameters that have the greatest effect on the differential's performance are friction coefficient, μ, and loss coefficient, η. The friction coefficient, μ, sets the maximum force F that can be transmitted before wheel slippage according to the equation $F = \mu N$, wherein N is the normal force that we set as a preload on the differential. The loss coefficient, η, measures the fraction of energy lost to elastic hysteresis when a material is stressed and relaxed. Higher η equates with higher energy loss. As the wheels roll, the moving contact point compresses and uncompresses, losing energy in each strain cycle. According to Ashby [9], rubbers have the highest loss coefficient, on the order of 1 to 3, and metals have much lower coefficients, on the order

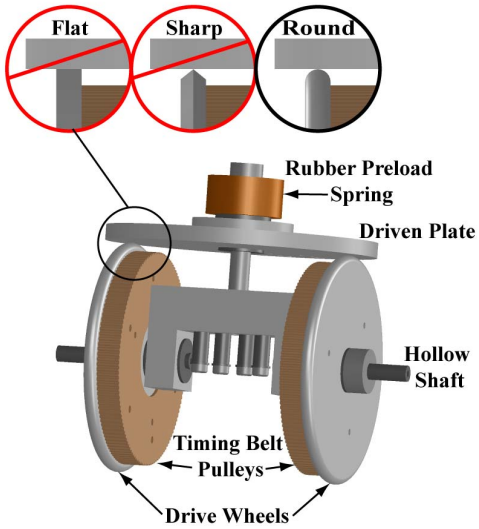

Fig. 4: The aluminum-aluminum friction differential mechanism. A rounded profile is optimal.

of 10^{-4} to 10^{-3} for steel and aluminum. Although rubber-metal is a popular material combination for friction drives due to the high μ, on the order of 1 to 4, the high loss coefficient in the rubber makes the transmission feel lossy and is unsuitable for haptics. Aluminum-on-aluminum is an optimal selection because it provides the highest μ, 1.35 for dry contact [10], of any metal-on-metal contact with nearly the lowest η of all metals [9].

We experimented with texturing the surface of the driven plate to raise the friction coefficient, and hence torque transfer capacity. However, the texturing in our prototypes introduced significant forces that distorted force renderings.

A 3D accelerometer is used to home the pitch and yaw degrees of freedom to an absolute position. The accelometer gives us the added ability to detect slippage in the friction differential, as well as the possiblity of improved dynamics. In the future, we plan to use the accelerometer and an inertial model of the device to cancel some of the inertial forces of the device through feed-forward control.

B. Radial DOF

The radial degree of freedom consists of a grounded motor, a cable transmission, and a linear slide. The cable routes from a Maxon RE-25 at the base of the device through the differential mechanism to the head of the linear slide, upon which sits the gimbal. Details of the cable routing implementation are shown in Figure 5, and the entire cable loop is shown in Figure 6. As with the pitch/yaw motors, grounding the radial-DOF motor reduced inertia and increased compactness near the user's hand significantly. A US Digital 1250 CPR encoder provides a linear resolution of 7.5 μm.

For reasons that will be discussed later, the cable must be routed as close to the rotational axes and center of rotation of the differential as possible. Nine redirect pulleys are required to route the cable along this desired path from the motor to the linear guide-block, where both cable ends terminate.

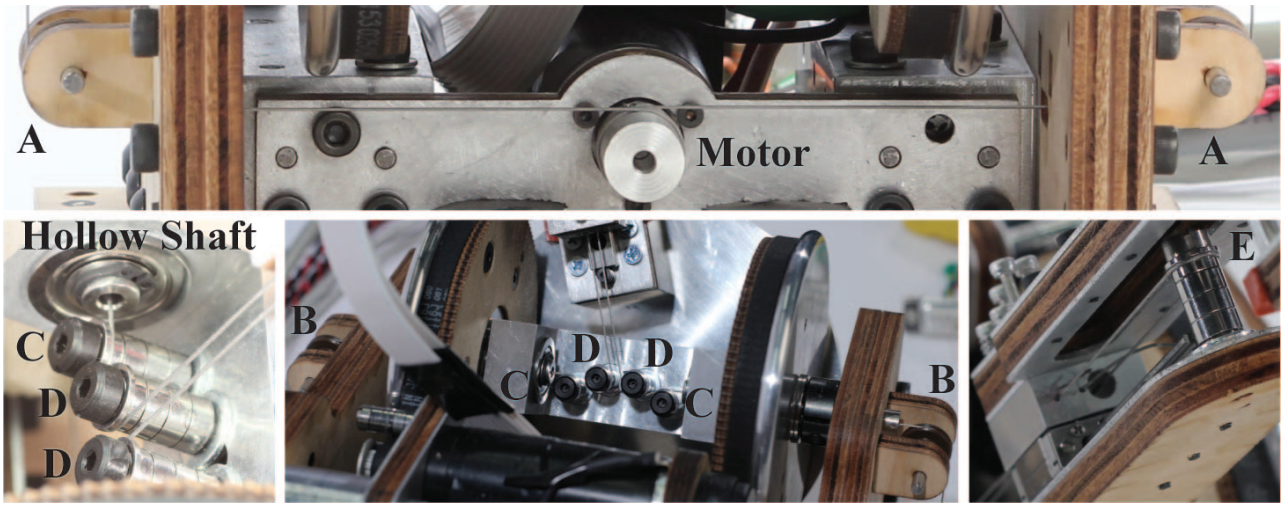

Fig. 5: Closeups of routing the cable for the radial DOF.

The pulley configuration is identical for both sides of the cable loop, with the exception of pulley E. Starting from the motor, pulleys A and B direct the cable to the outer entrance of the hollow differential shaft. Pulleys B and C direct the cable through the hollow differential shaft along its central axis. Pulley D redirects the cable to align with the radial direction. Pulley E redirects one side of the cable so that it can pull on the linear guide from above while the other side of the cable loop pulls on the linear guide from below. Because all of the pulleys are flanged and the fleet angles low, accidental decabling of the device has never been experienced. Installation of the cable is also exceedingly simple, requiring only a few minutes.

There are a few issues regarding cable placement that require special attention. Because the cable is a closed loop, its arc length must not change appreciably through the entire range of motion of the device. A change in arc length, ΔS, would result in a spring force that would tend to return the device to its lowest-energy configuration, thereby distorting the force renderings. To this end, we placed the cable as close to the rotational axes and center of rotation as possible. We were able to route the cable directly along the Y_0 axis as the cable passes through the hollow differential shafts. However, the cable could not be placed ideally once it redirected along the radial direction. Because there are two sides to the cable loop and only one radial path that passes directly through the differential's center of rotation, the cables are offset on either side of the center of rotation by a maximum of 1.5mm in the nominal configuration. Our final design has a total cable length of 795mm and a ΔS of 0.02mm, producing a strain of $2.5 \cdot 10^{-5}$ and a corresponding change in cable tension of 0.98N (0.22 lbf). While this configuration-dependent change in internal cable tension theoretically has a coupling effect on pitch and yaw, the small magnitude of the force and the small lever arm over which it acts render the coupling negligible.

There is a more significant coupling effect from the fact that actuation of the radial DOF requires a force to be applied offset of the differential's center of rotation, thereby inducing

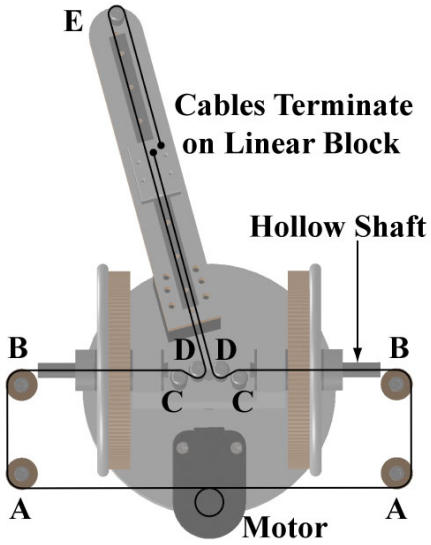

Fig. 6: Cable loop for radial DOF.

a coupling torque in the yaw DOF. If the radial DOF is driven at its maximum continuous motor torque, the torque induced in yaw is $7.28N \cdot mm$, or 6.3% of the friction torque in yaw, as discussed later in the paper. The induced torque at peak operation is $34.25N \cdot mm$, or 29.8% of the friction torque in yaw. Since the induced torque in yaw is such a small fraction of the friction in that DOF, coupling between the radial and yaw DOF cannot be felt practically.

The selection of the linear slide proved to be an interesting exercise. Because we wished for the slide to constrain rotation about its axis, we were unable to use traditional linear ball bearings or bushings. The remaining options were track-rollers, splines, ball-splines, and recirculating-ball linear guide-blocks/rails. We chose to use the linear guide-block/rail because it has the least backlash and friction in the smallest package of these options. However, an unintended consequence was that the recirculation of the balls produces

a noise that increases the perception of friction in the slide. The friction properties of the device feel significantly more isotropic when a user wears headphones than when able to hear the linear slide noise.

There are two potential drawbacks of our cable transmission design for the radial DOF. One is the range-of-motion achievable in yaw. Because the two sides of the cable loop draw nearer to each other in the same plane with increased rotation in yaw, eventually the cables will collide. For our final design, we would be able to rotate $\pm 42^\circ$ in yaw before experiencing cable collision. For applications that require a higher angular range-of-motion, we could eliminate this cable collision altogether by separating the two sides of the cable loop into two different planes when they redirect to the radial direction. This separation could be achieved by running the cable slightly off-axis of the hollow differential shafts and offsetting the flanges on pulleys C and D that redirect the cables along the radial direction.

Another potential issue is scalability. Our cable transmission design scales up very well but could have issues for very small designs (greater than a x2 size reduction). The robustness of reciprocating-ball linear guides is quite bad for the smallest of slides, requiring the use of an alternative, such as a spline. Great care would be needed to minimize backlash and friction in the spline, but this appears to be a viable option for much smaller versions of our device. Another limiting factor could be the fatigue life of the cable as the diameter of the redirect pulleys decreases. Experimenting with different cable constructions and materials could improve the fatigue life at small scales.

C. Wrist Gimbal

We developed a passive, 2-DOF gimbal and stylus to follow the pose of a user's hand (Figure 7). Note that since the attachment of the gimbal to the main 3-DOF device consists of only 4 screws, one could easily attach a custom gimbal with kinematics and actuation tailored to a specific application (e.g. the addition of active roll for laparoscopic simulation). The gimbal uses the same type of aluminum-on-aluminum friction differential as the main device to allow rotations about the wrist, with the exception of roll about the stylus. The gimbal's friction differential is 1/5 the size of the main friction differential, showing that the aluminum-aluminum friction differential design scales down well.

We sensed the position of each differential wheel via a secondary friction transmission to a 125-CPR incremental encoder. A section of thin silicone tubing pressed onto the shaft of the encoder allows for slight misalignment of the encoder shaft and differential wheel without losing contact. Measurement of the drive wheel position via this secondary friction transmission allows us to apply high loads to the well-supported gimbal differential without hurting the fragile encoder shafts. Another advantage is that we obtain a 1:7.5 gear ratio that improves the effective resolution. We achieve a resolution of 0.07° for both gimbal angles.

We use two small neodymium magnets, one stationary at the base of the gimbal and one attached to the base of the stylus, to home the gimbal with an absolute position. The magnets are placed below the natural workspace of the gimbal so that they do not interfere with normal operation, but do automatically guide the stylus to its homing position when the user lets go of the stylus. This allows for automatic homing of the gimbal with no required action by the user.

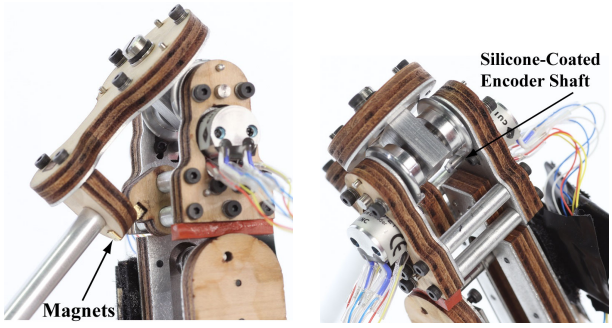

(a) (b)

Fig. 7: 2-DOF gimbal employing an aluminum-aluminum friction differential, a steel-silicone friction transmission to the encoders, and magnetic homing for absolute positioning

The gimbal suffers from a wrist-lock singularity when the stylus is aligned with the differential axis. Although the singularity is reachable within the gimbal's workspace, it rarely posed a problem when interacting with virtual models. We find that it is a good trade-off between the infrequent possibility of encountering this singularity and the simple, robust design of the friction differential.

IV. ANALYSIS OF DEVICE PROPERTIES

A. Weight, Workspace, and Spatial Resolution

Our device is comparable in size and weight to the Phantom Omni (Sensable Technologies, Willmington, MA). Our device weighs 2.5kgf (5.5lbf), whereas the Omni weighs 1.8 kgf (4.0 lbf). The workspace of our device comprises a segment of a spherical shell, as shown in Figure 3. The pitch ϕ is on the range $[-50^\circ, +30^\circ]$, and the yaw γ is on the range $[-25^\circ, +25^\circ]$. The radial DOF ρ spans 86.5mm, for an inner shell radius of 195.5mm and an outer radius of 282mm. For applications that lend themselves to spherical kinematics, such as laparoscopic simulation, but require a greater range of motion in pitch and yaw, a few adjustments to the motor placement and links allows for more than doubling of the angular range-of-motion. The trade-off for this expanded angular range-of-motion is a small increase (roughly 10% - 20%) in the footprint of the base. For general haptic applications, wherein rendering is expected to occur within a bounding box, we can fit a bounding box measuring 160mm x 120mm x 68mm into our workspace. For comparison, the stated bounding box of the Omni is nearly identical.

We computed the spatial resolution/quantization at our end-effector ΔX_{ee} by gridding the workspace W, computing the spatial resolution for each configuration $\mathbf{q}$, and taking the worst-case (least-precise) resolution/quantization.

$$\Delta X_{ee} = \max_{\mathbf{q}\in W}\{||J(\mathbf{q})\delta_{\mathbf{q_{min}}}||\},\ \ \delta_{\mathbf{q_{min}}} = \begin{bmatrix} 2.8\cdot 10^{-4} \\ 2.8\cdot 10^{-4} \\ 7.5\cdot 10^{-3} \end{bmatrix} \quad (1)$$

where $\delta_{\mathbf{q_{min}}}$ is the vector of joint resolutions set by our encoders' precision. We obtained a worst-case resolution of 0.112mm across the entire workspace. The resolution is linearly dependent upon ρ, but is almost constant across pitch and yaw (0.1098 $\pm$ 0.0016mm across all pitch, yaw for ρ = max extension). For comparison, the Sensable Phantom Omni is somewhat more precise than our device, with a best-case spatial resolution of 0.055mm, or 49% of our resolution.

B. Forward Kinematics

The transformation between motor angles/torques and pitch, yaw angles/torques on the differential plate is:

$$\phi = \frac{(\theta_{motor1} + \theta_{motor0})}{2N},\ \gamma = \frac{(\theta_{motor1} - \theta_{motor0})}{2N}\frac{d}{D} \quad (2)$$

$$\tau_\phi = N(\tau_{motor1} + \tau_{motor0}),\ \tau_\gamma = N(\tau_{motor1} - \tau_{motor0})\frac{D}{d} \quad (3)$$

$$\tau_{motor0} = \frac{1}{2N}(\tau_\phi - \tau_\gamma\frac{d}{D}),\ \tau_{motor1} = \frac{1}{2N}(\tau_\phi + \tau_\gamma\frac{d}{D}) \quad (4)$$

where $\frac{d}{D}$ is the ratio between drive wheels diameter d and distance between the drive wheels D, and N is the gear ratio between the motors and differential drive wheels. In our case, $\frac{d}{D} = 1$, and N is 10.83.

The forward kinematic transformation from the end effector frame to the world frame is

$${}^0T^3 = \begin{bmatrix} \mathrm{C}_\phi & \mathrm{S}_\phi\mathrm{S}_\gamma & \mathrm{S}_\phi\mathrm{C}_\gamma & (\rho+R_e)\mathrm{S}_\phi\mathrm{C}_\gamma \\ 0 & \mathrm{C}_\gamma & -\mathrm{S}_\gamma & -(\rho+R_e)\mathrm{S}_\gamma \\ -\mathrm{S}_\phi & \mathrm{C}_\phi\mathrm{S}_\gamma & \mathrm{C}_\phi\mathrm{C}_\gamma & (\rho+R_e)\mathrm{C}_\phi\mathrm{C}_\gamma \\ 0 & 0 & 0 & 1 \end{bmatrix} \quad (5)$$

C. Jacobian and Singularities

The Jacobian for linear motions at the end-effector is

$${}^0J_v = \begin{bmatrix} (\rho+R_e)\mathrm{C}_\phi\mathrm{C}_\gamma & -(\rho+R_e)\mathrm{S}_\phi\mathrm{S}_\gamma & \mathrm{S}_\phi\mathrm{C}_\gamma \\ 0 & -(\rho+R_e)\mathrm{C}_\gamma & -\mathrm{S}_\gamma \\ -(\rho+R_e)\mathrm{S}_\phi\mathrm{C}_\gamma & -(\rho+R_e)\mathrm{C}_\phi\mathrm{S}_\gamma & \mathrm{C}_\phi\mathrm{C}_\gamma \end{bmatrix} \quad (6)$$

A singularity exists when $\gamma = \pm\frac{\pi}{2}$, but these configurations are outside of the device's workspace.

D. Gravity Compensation

We use active, feed-forward gravity compensation so that the device floats in all configurations without being a burden on the user's hand. The 3D CAD model provides an accurate mass model of the device. The joint-space gravity torque vector ${}^0\tau_g$ is:

$${}^0\tau_g = \begin{bmatrix} \tau_\phi \\ \tau_\gamma \\ F_\rho \end{bmatrix} = g\begin{bmatrix} -m_1X_1\mathrm{C}_\phi - m_2(X_2\mathrm{C}_\phi + Z_2\mathrm{C}_\gamma\mathrm{S}_\phi) - m_3(\rho+R_C)\mathrm{C}_\gamma\mathrm{S}_\phi \\ \mathrm{C}_\phi\mathrm{S}_\gamma(-m_2Z_2 - m_3(\rho+R_C)) \\ m_3\mathrm{C}_\phi\mathrm{C}_\gamma \end{bmatrix} \quad (7)$$

where m_1 = 0.13kg, m_2 = 0.33kg, m_3 = 0.08kg, X_1 = 11.23mm, X_2 = 41.69mm, Z_2 = 20.51mm, and R_C = 132.48mm.

E. Maximum Isotropic Force

A practical metric for evaluating the force capabilities of our device is the maximum isotropic force over the workspace, or the largest force that can be exerted in all directions and kinematic configurations before any motors saturate. For a configuration, we find the minimum force magnitude f_u that will saturate any of the motors across all directions $\mathbf{U}$. The torque vector $\bar{\tau}$ that will result in the largest force $F_{Max\ Iso}$ before any of the motors saturate is:

$$\bar{\tau} = \arg\min_{\mathbf{U}\in\Re}\{max(\tau_i/\tau_{SAT\,i}) \mid f_u\mathbf{U} = \bar{J}\bar{\tau}\},\ \ F_{Max\ Iso} = \bar{J}\bar{\tau} \quad (8)$$

where $\tau_{SAT\,i}$ is the saturation torque for each motor, indexing on i. We solved for $F_{Max\ Iso}$ computationally by gridding the workspace with finite configurations, gridding force directions at each configuration, and incrementally increasing the force magnitude f_u until one of the motors saturates for a given configuration and force direction $\mathbf{U}$. Figures 8(a)-(b) show the maximum force in all directions for an example configuration. Despite the rough appearance due to sampling, the surface has 6 sides corresponding to the the forward and reverse saturation of each motor. Figures 8(c)-(f) show the maximum isotropic force at each configuration across the workspace. Without gravity compensation, the maximum force is roughly constant across all ϕ, γ and decreases linearly with increasing ρ. The use of active gravity compensation decreases the maximum isotropic force because some of the rendering force is used to counter gravity. Gravity compensation also makes the maximum isotropic force significantly more configuration-dependent, with the highest available forces corresponding to low values of yaw and negative values of pitch.

Table I lists the maximum isotropic force that the device can exert across its workspace (the minimum value shown in Figures 8(c)-(f)). The values are tabulated for combinations with and without gravity compensation, as well as motor saturation at $\tau_{continuous}$ (maximum continuous torque) and τ_{peak} (intermittent, peak torque). Note that the stated maximum continuous force for the Sensable Phantom Omni is 0.88 N, a value which is only 7% higher than our maximum continuous isotropic force with gravity compensation (our worst case). Since the Omni is typically used without gravity compensation, by practical comparison, our device is able to produce 82% higher maximum continuous force.

Peak forces can be achieved by overdriving the motors intermittently, according to the manufacturer's thermal specifications. For example, the motors could be run at 100% τ_{peak} (4.7 x $\tau_{continuous}$) for durations of up to 0.48S with a 5.2% duty cycle or at 50% τ_{peak} (2.6 x $\tau_{continuous}$) for durations of up to 2.09S with a duty cycle of 53.5%.

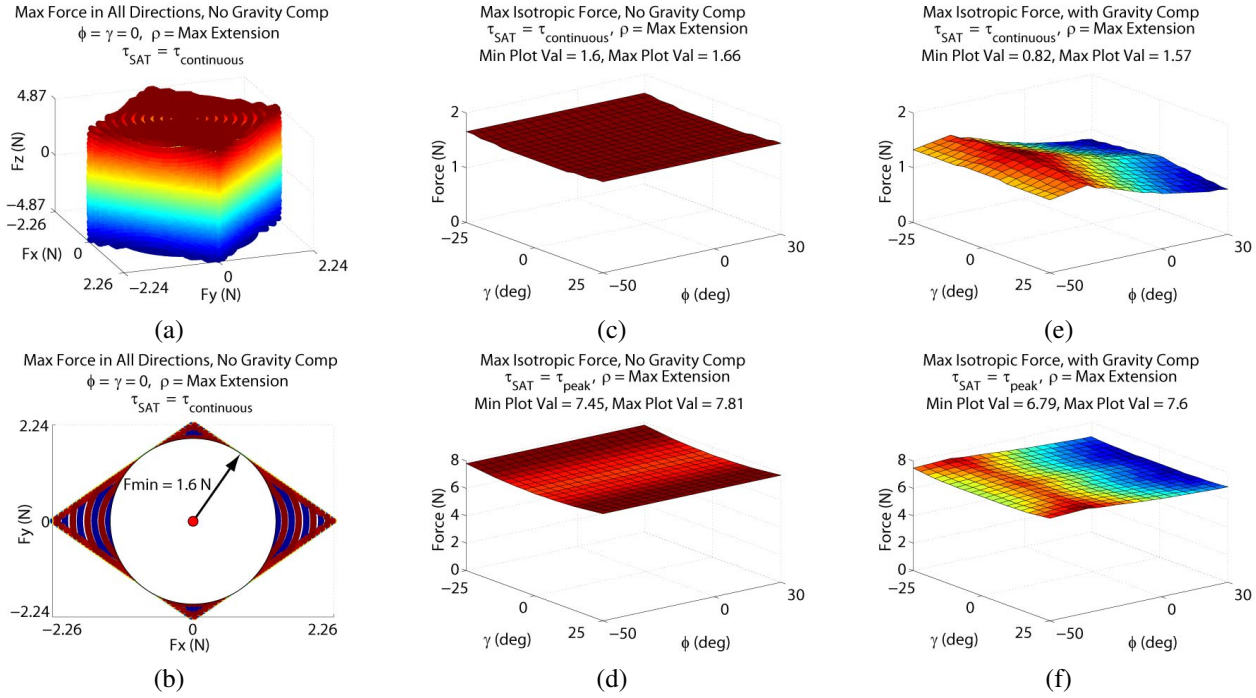

Fig. 8: (a) Maximum force in all directions at a particular configuration. The maximum isotropic force for this configuration is determined by the largest sphere that fits within this bounding surface. (b) Projection onto the X-Y plane of the maximum force in all directions. (c)-(f) Maximum isotropic force across workspace.

TABLE I: Maximum Isotropic Force Across Workspace

	$\tau_{SAT} = \tau_{continuous}$	$\tau_{SAT} = \tau_{peak}$
Without Gravity Comp.	1.60N	7.45N
With Gravity Comp.	0.82N	6.79N

F. Friction

We measured the back-drive friction for each DOF by hanging proof-weights to pull at the end-effector (center of the gimbal) until movement was achieved. Table II lists the maximum friction torque and friction force at the end-effector measured for each DOF:

TABLE II: Friction Measurements, Maximum Values

	torque (N·mm)	$F_{\text{wrist, retracted}}$ (N)	$F_{\text{wrist, extended}}$ (N)
pitch (ϕ)	67.1	0.34	0.24
yaw (γ)	115	0.59	0.41
radial (ρ)	n/a	0.93	0.93

Friction force in pitch and yaw decreases linearly with radial extension because the lever-arm over which the friction torque acts is increasing. Friction in the radial degree-of-freedom is configuration-independent. Friction in the pitch DOF is lower than in yaw because pure pitch motion rotates the entire differential about the Y_0 axis without any differential rotation of the drive wheels. That is, pitch motion feels only friction in the main support bearings and belts. Pure yaw motion requires differential motion of the drive-wheels, thereby adding their rolling friction as well. The radial DOF experiences the highest friction due to the reciprocating-ball linear slide and the energy lost to the nine redirect pulleys required to route the cable through the differential mechanism. The anisotropic friction is not readily noticable when in contact with a virtual object but can be felt somewhat in free-space.

G. Dynamic Range

We compute the dynamic range of the device as the ratio of the maximum isotropic force to the friction. Since the friction is anisotropic, we have computed the minimum and maximum dynamic range based on the minimum and maximum friction. Table III shows the minimum and maximum dynamic range both with and without gravity compensation. The minimum case is when the device is in the nominal configuration and pushing in the X_0 direction, thereby experiencing friction only in the pitch ϕ DOF. The maximum case is when the device is in the nominal configuration and pushing in the Z_0 direction, thereby experiencing friction only in the radial ρ DOF. Clearly, the radial DOF sets the lower bound for the overall dynamic range of the device. In comparison with our device, the Sensable Phantom Omni has a stated maximum force of 3.3N and a backdrive friction of 0.26N, for a dynamic range of 12.7.

TABLE III: Dynamic Range

	With Gravity Comp.	Without Gravity Comp.
Min (force in Z_0)	7.3	8.0
Max (force in X_0)	28.3	31.0

H. Effective Mass

Dynamic analysis of this device is more complicated than a simple serial mechanism. The differential drive wheels and motors contribute to the inertia of both rotational DOFs, and the mass of the radial link is non-isotropic due to the motor rotor inertia. As a result, we computed the mass matrix by first computing the kinetic energy of the device, including the contributions from the motor rotors, and then computationally solving for the cartesian-space mass matrix Λ_e as the effective mass at the end-effector.

Our device has fairly isotropic operational-space mass properties throughout its workspace, so a user will not notice significant variability in inertial resistance/back-drivability. That is, the low and isotropic effective mass of our device will make free-space feel free.

Figure 9 plots the effective mass

$$\frac{1}{m_{\mathbf{u}}(\Lambda_e)} = \mathbf{u}^T \Lambda_e^{-1} \mathbf{u} \tag{9}$$

in every direction $\mathbf{u}$ for some key device configurations. In the nominal position, Λ_e is nearly isotropic:

$$\Lambda_{e|\phi=0,\gamma=0,\rho=0} = \begin{bmatrix} 0.083 & 0 & 0 \\ 0 & 0.096 & 0 \\ 0 & 0 & 0.118 \end{bmatrix} kg \tag{10}$$

There is only a 42% spread between minimum and maximum diagonal values. In the fully extended nominal position, the result is:

$$\Lambda_{e|\phi=0,\gamma=0,\rho=max} = \begin{bmatrix} 0.073 & 0 & 0 \\ 0 & 0.080 & 0 \\ 0 & 0 & 0.118 \end{bmatrix} kg \tag{11}$$

for a 61% spread. We see that extending the radial link makes the ellipsoid of effective mass less isotropic; m_{X_0} and m_{Y_0} decrease by 12% and 17%, respectively, but m_{Z_0} remains unchanged.

Due to the spherical nature of the device, changes in pitch or yaw configuration have minimal impact on the effective mass. While the principal directions of Λ_e change, the magnitudes change by less than 3%. Note that the stated effective mass of the Sensable Phantom Omni is 0.045kg, or 38% of our maximum/54% of our minimum effective mass.

V. CONCLUSIONS AND FUTURE WORK

A. Conclusions

In this paper, we presented a new transmission design for a spherical haptic device with pitch, yaw, and radial DOF. By grounding all motors in the base, we achieved a scalable design with a slim form factor and low-inertia. Our novel contribution is the design of an aluminum-aluminum friction differential and cable transmission that routes through the differential to a prismatic, radial DOF. This design is simple, easily fabricated, and reliable. Our device is an improvement on existing devices for specific applications that require spherical kinematics with a radial DOF, and its workspace and force capabilities make it useful for general rendering.

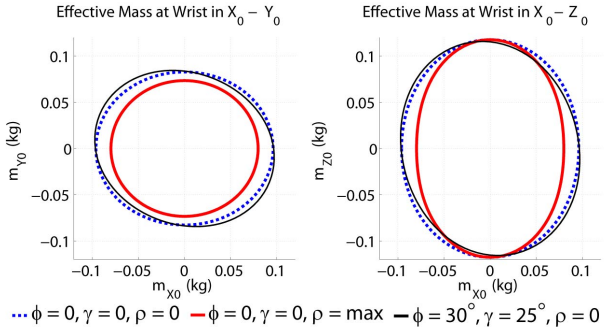

Fig. 9: Effective mass at the wrist point for three configurations. The effective mass is not heavily influenced by configuration throughout the workspace.

B. Future Work

To improve the maximum force to back-drive inertia ratio, we plan to replace the motors with Maxon RE-30's and use smaller gear ratios in the belts/cable. The main drawback of this device is the anisotropic friction in the radial DOF. The bulk of the friction and noise is generated in the reciprocating-ball linear guide-block, and we plan to investigate alternatives, including linear air bearings, to reduce this. We plan to explore other possible applications for our design, including as the shoulder in a robot arm wherein multiple cables could be routed through the friction differential to actuate additional joints.

VI. ACKNOWLEDGMENTS

R. Brewer and A. Leeper are both supported by National Science Foundation GRFP Fellowships.

REFERENCES

[1] Y. Han, P. Kang, K. G. Sung, and S. B. Choi, "Force feedback control of a medical haptic master using an electrorheological fluid," *J. of Intelligent Material Systems and Struct.*, vol. 18, pp. 1149–1154, 2007.

[2] L. Birglen, C. Gosselin, N. Pouliot, B. Monsarrat, and T. Laliberté, "Shade, a new 3-dof haptic device," *IEEE Transactions on Robotics an Automation*, vol. 18, no. 2, pp. 166–175, 2002.

[3] T. Massie and J. K. Salisbury, "The phantom haptic interface: A device for probing virtual objects," *Proceedings of the ASME Winter Annual Meeting, Symposium on Haptic Interfaces for Virtual Environment and Teleoperator Systems*, pp. 295–301, 1994.

[4] S. Grange, F. Conti, P. Helmer, P. Rouiller, , and C. Baur, "The delta haptic device," *Eurohaptics*, 2001.

[5] M. Smith, "Tactile interface for three-dimensionsal computer-simulated environments: Experimentation and the design of a brake-motor device," MS Thesis, Massachusetts Inst. of Technology, 1988.

[6] M. Russo, "The design and implementation of a three degree of freedom force output joystick," MS Thesis, Massachusetts Institute of Technology, 1990.

[7] U. Spaelter, T. Moix, D. Ilic, H. Bleuler, and M. Bajka, "A 4-dof haptic device for hysteroscopy simulation," *IEEE/RSJ International Conference on Intelligent Robots and Systems*, pp. 3257–3263, 2004.

[8] P. Gregorio, N. Olien, D. Bailey, and S. Vassallo, "Interface apparatus with cable-driven force-feedback and four grounded actuators," U.S. Patent 7 404 716, 2008.

[9] M. Ashby, *Materials Selection in Mechanical Design*, 3rd ed. Elsevier, 2005, p. 62.

[10] E. Oberg, F. Jones, and H. Horton, *Machinery's Handbook*, 21st ed. Industrial Press Inc., 1981, p. 546.